VOLUME 36 JOURNAL OF METEOROLOGICAL RESEARCH APRIL 2022

Factors Influencing Diurnal Variations of Cloud and Precipitation in the Yushu Area of the Tibetan Plateau

Bangjun CAO, Shihua LYU, Yu ZHANG*, Xianyu YANG, Boliang LI, Liang YUAN, and Meilin LI

Plateau Atmosphere and Environment Key Laboratory of Sichuan Province, School of Atmospheric Sciences, Chengdu University of Information Technology, Chengdu 610225

(Received September 22, 2021; in final form January 13, 2022)

ABSTRACT

Using the cloud radar, ground observations, and ECMWF Reanalysis v5 (ERA5) data, we investigate the factors influencing nighttime precipitation during summer in the Yushu area of the Tibetan Plateau (TP). The cloud top height (CTH), cloud base height (CBH), and liquid water content (LWC) are compared between non-precipitation and precipitation days. The results show that the average CTH on precipitation days in Yushu is below 10 km above ground level (AGL) in the daytime, whereas it exceeds 10 km AGL at night, with the maximum at 2300 BT (Beijing Time). The CBH is in-phase with the dewpoint spread. The precipitation intensity and CTH are in-phase with the LWC. The hourly averaged precipitation intensity and convective available potential energy in ERA5 reach their maximums at 2100 BT, which is 3 h ahead of their observed counterparts. There is descending motion in the mid day on non-precipitation days, whereas there is ascending motion at night on precipitation days. In addition, the horizontal wind direction in the lower level (below 5000 m) shows clockwise rotation from morning to night. Wind shear occurs in the mid level of the atmosphere, accompanied by a subtropical westerly jet in the upper level. The difference in horizontal wind speed between 200 and 500 hPa is positively related to the LWC, thereby contributing to the formation of upper-level cloud.

Key words: diurnal variation, cloud, precipitation, Tibetan Plateau

Citation: Cao, B. J., S. H. Lyu, Y. Zhang, et al., 2022: Factors influencing diurnal variations of cloud and precipitation in the Yushu area of the Tibetan Plateau. *J. Meteor. Res.*, **36**(2), 311–325, doi: 10.1007/s13351-022-1167-6.

1. Introduction

The Tibetan Plateau (TP), located in Southwest China (26°00′–39°47′N, 73°19′–104°47′E), is often referred to as the “roof of the world” owing to its average elevation exceeding 4000 m. The meridional monsoonal circulation generated by the thermal and dynamic effects of the TP causes the Hadley circulation to break down in the Asian monsoon region, which enables water vapor from the tropics and equator to enter subtropical and even mid–high-latitude East Asia (Fu et al., 2020). The TP plays a key role in the formation of the Meiyu rain band in the Yangtze River basin in summer by serving as a “transfer station” for water vapor from low-latitude areas (Tao and Ding, 1981). In addition, the TP transports a substantial amount of heat and water vapor into the atmosphere as a rising heat source (Fu et al., 2006). The special dynamic and thermal effects of the TP make an important contribution to the onset and maintenance of the Asian monsoon, and therefore influence the occurrence of disastrous weather around the plateau and its downstream areas (Fu et al., 2006; Xu et al., 2008). The TP is also often referred to as Asian “water tower” owing to the major river systems of the continent originating in the TP region. Since the late 1970s, the climatic effects of the TP have been widely studied. Researchers have conducted several scientific experiments in the TP region—for example, GEWEX Asian Monsoon Experi-

---

Supported by the Second Tibetan Plateau Scientific Expedition and Research Program (2019QZKK0102), National Natural Science Foundation of China (41975130 and 42005072), National Key Research and Development Program of China (2018YFC1505702), and Sichuan Provincial Innovation Training Program for College Student (S202010621048 and S202110621004).

*Corresponding author: yuzhang@cuit.edu.cn

ment in Tibet (GAME-Tibet; Uyeda et al., 2001), the First Qinghai–Xizang Plateau Meteorological Experiment, and the Second and Third Tibetan Plateau Atmospheric Experiments (Zhao P. et al., 2017).

The precipitation amount and frequency often show a bimodal pattern diurnally, peaking in the morning and evening, with the greatest change occurring over the mid TP (Fujinami and Yasunari, 2001; Feng et al., 2002; Bai et al., 2008; Feng and Wei, 2008; Ji et al., 2017). The diurnal variation of precipitation in the TP region in summer has its minimum in the morning and maximum at 2000 BT (Beijing Time) (Liu et al., 2002). The convective activity and the precipitation amount and frequency begin to increase dramatically after 1200 LT (local time), up to a maximum value in Naqu of the mid-west TP at 1800 LT (Chang and Guo, 2016). After nightfall, stratiform-cloud precipitation occurs and lasts to 0600 LT, and then disappears gradually. The eastern TP foothills are dominated by nocturnal rainfall before midsummer (Xu and Zipser, 2011). However, Feng et al. (2002) showed that the convective activity reaches a maximum at 1400 LT and that the diurnal change in precipitation shows four peak values.

The linkages between precipitation over the TP and local or nonlocal factors have been investigated. The diurnal variations of monsoonal flow, sea–land breeze, boundary-layer flow, and low-level jet are the key factors that influence the diurnal variation of precipitation over the East Asian summer monsoon (EASM) region (Gong et al., 2004; Chen et al., 2009; Yu et al., 2014). The spatial distribution of summertime precipitation is related to the moisture transport controlled by the weather systems around the TP (Feng and Wei, 2008). Recently, the impact of aerosol on the weather and climate over the TP has been investigated, revealing that aerosol pollutants can pass over the Himalayan mountains and reach the internal regions of the TP, causing impacts on the formation and development of clouds and precipitation there (Zhao et al., 2020). Numerous simulations have shown that the mid-level horizontal wind field in the mid troposphere (500 hPa) shows inertial oscillation (e.g., Li et al., 2021). In addition, most of the nocturnal precipitation is in-phase with mesoscale convective systems and is possibly contributed by long-lived occurrences of such systems evolving from late-afternoon or early-evening convection (Xu and Zipser, 2011). The diurnal variation of cloud and precipitation is related to the diurnal variation of thermal parameters at Naqu (Liu et al., 2002; Zhao C. F. et al., 2017). The diurnal change in convective available potential energy (CAPE) is in-phase with that of precipitation, but it contrasts with that of the lifting condensation level (LCL) after the onset of the EASM (Liu et al., 2002). The atmospheric layer between 6 and 8.5 km at most times of the day is unstable, whereas below 6 km and above 9 km at 0400–0800 BT, it prevents the development of convection.

In addition, the cloud base height (CBH) and cloud top height (CTH) over the TP and their influencing factors have been investigated. After the EASM over the TP, the CTH usually exceeds 16 km above mean sea level (MSL), sometimes exceeding 20 km MSL (Zhao et al., 2019; Yang et al., 2020). The average CBH during summer over the TP exceeds 1.5 km above ground level (AGL), which is larger than that over the plains and Sichuan Basin. The average CTH is about 10 km AGL during deep convective precipitation in the TP region, in which solid particles account for a large proportion (Fu et al., 2020). About 70% of the convective precipitation over the TP has an average height of 8–12 km AGL, which is higher than that in other parts of Asia in the same period. The precipitation over the TP is dominated by deep, weak convective precipitation in summer, and these deep precipitation systems move eastwards over the plateau (Fu et al., 2020). The factors influencing the CBH have also been investigated. Craven et al. (2002) demonstrated that the CBH shows good agreement with the LCL calculated from the surface layer, and Romps (2017) investigated the dependence of the LCL on the relative humidity and temperature. The relative humidity in the cloud layer is significant in determining the CBH (Zhang and Klein, 2013; Wang Y. et al., 2018), and ground-based radar observations over Naqu in July 2014 (Zhao C. F. et al., 2017) showed that there were many clouds with bases below 1.2 km AGL. Wu et al. (2015) found three major "conveyer belt" branches of water vapor over the TP: the first is in the tropics across the Arabian Sea, Bay of Bengal, and South China Sea; the second flows northwards across northern India and the Bay of Bengal towards the southern slopes of the TP; and the third transports water vapor to sustain the EASM.

Numerical simulation results reported by Li et al. (2021) indicated that the maximum CAPE occurred in the early evening at 1800 BT, which is different from the findings of Liu et al. (2002). Almost all of the global climate models that participated in phase 5 of the Coupled Model Intercomparison Project overestimated the climatological annual mean precipitation over the TP owing to a wet bias (Su et al., 2013). The precipitable water vapor in current models is higher and its diurnal variation stronger than observations over the southern TP (You et al., 2015; Wang Y. et al., 2018). This phenomenon can be related to the coarse resolutions of numerical models, which means that they are unable to resolve the complex terrain. Improving the model resolution (Li et al., 2021), drag parameterization scheme (Beljaars et al., 2004; Zhou et al., 2018), and freeze–thaw scheme (Wang et al., 2003; Yang and Wang, 2019) could improve the accuracy of precipitation simulation.

Based on the literature reviewed above, we can see that a great deal of uncertainty remains in the diurnal cycle from model data, satellite data, and station observations in the TP region. There is a lack of observed cloud and precipitation radar data, and little relevant research over northeastern TP where the topography is mainly composed of mountains, valleys, and plains. Our level of understanding with respect to the factors influencing cloud and precipitation is insufficient. For instance, what are the factors that determine the diurnal variations of CBH and CTH under different weather conditions, including sunny and rainy days? What is the relationship between the precipitation and CAPE, vertical velocity, and water vapor transport?

To improve our understanding of the mechanism of precipitation over the northeastern TP, this paper analyzes the diurnal variation of the precipitation, CBH, and CTH using data observed by the Ka-band millimeter-wave cloud radar and raindrop spectrometer in the Yushu area of the TP, along with ECMWF Reanalysis v5 (ERA5) data. The relationship between the precipitation and several key factors such as CAPE, vertical velocity, and LWC are discussed. The question why the convective activity is stronger at night in this region is answered. This research is important for improving our understanding of the characteristics of weather systems in the northeastern TP, as well as for advancing our ability to forecast precipitation in this region.

2. Observation site and data

2.1 *Observation site and instruments*

To improve the parameterization of land surface, boundary layer, and cloud microphysical processes, observations of cloud microphysics are carried out by a research program entitled "The interaction between the earth and atmosphere of the TP and its influence on the weather and climate in the downstream." The observation period is from 1 July to 31 August 2019. One of the observation sites is Yushu National Standard Weather Station (33°41′N, 97°41′E) in the southwest of Qinghai Province. The terrain is predominantly mountain plateau, with an average altitude of 4449.4 m, and the topography is mainly composed of mountains, valleys, and plains. The area has a plateau cold-zone-type climate, with an average annual temperature of 2.9°C and annual precipitation of 487 mm, and the land cover includes arable land, grassland, and forest (Fig. 1).

The instruments used during this research program include a ground meteorological observatory, a Ka-band millimeter-wave cloud radar, and a ground raindrop spectrometer. All instruments are located at Yushu station. The Ka-band millimeter-wave cloud radar has an operating frequency of 33.44 GHz, and the variables detected by the radar include equivalent reflectivity factor, radial velocity, velocity spectral width, linear depolarization ratio, and energy spectral density. The vertical height of detection ranges from 120 to 15,000 m. The vertical resolution is 30 m, and the temporal resolution of the output data is 8.5 s. Based on these observations, we obtain the CBH, CTH, cloud thickness, cloud cover, and LWC. The LWC is retrieved by using the cloud radar data with the equation $\mathrm{LWC} = 3z^{0.5}$, where LWC is a

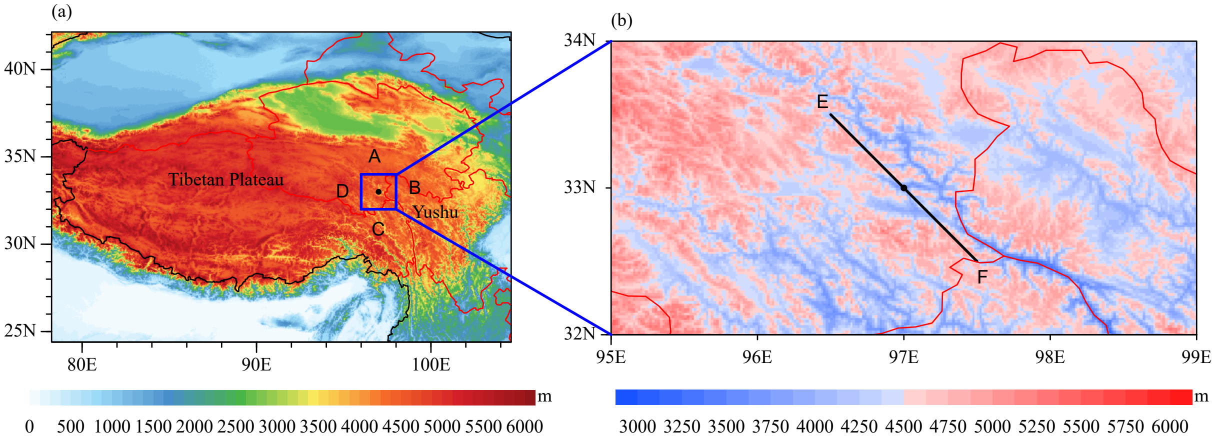

Fig. 1. Elevations of (a) the Tibetan Plateau and (b) Yushu area and the location of cross-section E–F. The blue rectangle ABCD signifies the Yushu area and encloses the control volume for budget analysis in this paper. The black dot is the observation site at Yushu.

power relationship with reflectivity z. For details about the cloud radar instrument and the cloud radar LWC retrievals, it can be seen in Zhao et al. (2012) and Cadeddu et al. (2013).

The ground-level raindrop spectrometer has a wavelength of 650 nm and a frequency of 50 kHz. The measurement range is 0.2–5.0 mm for liquid particles and 0.2–25 mm for solid particles, and it has 1024 particle grades (32 diameters × 32 speeds). The temporal resolution is 60 s. The instrument is able to obtain the precipitation intensity and precipitation frequency. The horizontal scale represented by the cloud radar observations can be assumed to be similar to that of the surface rainfall and temperature observations, because the surface rainfall and temperature observations and cloud radar are at the same location.

2.2 *ERA5 data*

We obtained the temperature, u, v, humidity, geopotential height, boundary layer height (BLH), and CAPE from the ERA5 hourly reanalysis dataset from 1 July to 31 August 2019, as well as monthly averaged reanalysis data from July to August 2019. The data can be downloaded from https://www.ecmwf.int/en/forecasts/datasets/reanalysis-datasets/era5. ERA5 has been widely used in various studies (Sun and Zhao, 2020; Xia et al., 2021). BLH was obtained from the ERA5 hourly dataset at the surface with a 1-h temporal resolution. In ERA5, BLH is defined as the height at which the bulk Richardson number is 0.25 (Troen and Mahrt, 1986). Guo et al. (2021) evaluated the BLH from ERA5 using sounding observations. CAPE in ERA5 is estimated by considering parcels of air departing at different model levels below 350 hPa. CAPE is an indication of the instability (or stability) of the atmosphere, which is related to the maximum potential vertical velocity of air within an updraft. In addition, CAPE can be used to evaluate the potential for the development of convection. Higher CAPE suggests greater potential for severe weather. To match the ground observations with ERA5 data in spatial terms, four grid values from the ERA5 reanalysis dataset that are near to the ground observations, including precipitation and BLH at one level and wind speed and air temperature at different levels, are bilinearly interpolated to produce the values at the observation site (Chen et al., 2014; Wang et al., 2014). The temporal resolution for the surface rainfall and temperature observations from the China Meteorological Administration and the data from ERA5 is 1 h. The cloud radar and raindrop spectrometer observations are averaged to 1 h. Therefore, the site-based precipitation is temporally matched with the cloud radar.

3. Methods

To investigate the cloud and precipitation characteristics, the observation days from 1 July to 31 August are divided into precipitation versus non-precipitation days. The precipitation days are defined as days on which the measurement of precipitation by the ground-level raindrop spectrometer is larger than 0.02 mm h^{-1}. The remaining days are then defined as the non-precipitation days. The number of precipitation days is 35, and the number of non-precipitation days is 27. The number of hours with precipitation at each hour during the diurnal cycle is used, which is defined as the number of all hours during the observation period when the precipitation observed by the raindrop spectrometer is larger than 0.02 mm h^{-1}. The standards for heavy rain (50–100 mm day^{-1}) and extreme rain (> 100 mm day^{-1}) are defined according to the standards of operational prediction in China (Chen et al., 2012). In addition, to investigate the water vapor transport, four boundary water vapor fluxes and net water vapor fluxes in the control volume for budget analysis composed of four planes (A, B, C, and D in Fig. 1) are calculated (Zhang et al., 2019). The water vapor flux is calculated as follows:

$$F = \int_{z_s}^{z_t} \int_{x_1}^{x_2} \rho q_v V_n \mathrm{d}x \mathrm{d}z, \tag{1}$$

where ρ, q_v, and V_n are the air density, water vapor mixing ratio, and velocity entering the boundary, respectively. The integral is the boundary length from x_1 to x_2, and the height from the surface z_s to the height $z_t = 15$ km (Fig. 1). The water vapor flux across planes A, B, C, and D in Fig. 1 is calculated. To investigate the factors influencing the CBH, dewpoint spread is also calculated, which refers to $T - T_d$, where T is the temperature at 2 m and T_d is the dewpoint temperature at 2 m.

4. Results and discussion

4.1 *Diurnal variation of cloud and precipitation at Yushu*

The daily precipitation rate on all days during the observation period is less than 20 mm day^{-1}, except on one day when it is between 20 and 25 mm day^{-1} (Fig. 2a). Therefore, there is no heavy rain during the observation period that might affect the statistical analysis that follows. The precipitation intensity reaches a maximum (0.4 mm h^{-1}) at 2200 BT, and its standard deviation is also the largest (Figs. 2b, c). The minimum precipitation intensity reaches at 0700 BT. The maximum number of precipitation hours in a day during the observation period is 13 at 2300 BT, and the minimum number of precipitation hours is only 4 at 1300 and 1500 BT (Fig. 2d). Taken together, the precipitation intensity and the number of precipitation hours are most prominent during the period from sunset to midnight.

The precipitation in ERA5 is compared with the observations in Figs. 2a–c. When the precipitation rate is less than 10 mm day^{-1}, the ERA5 precipitation rate is greater than that in the observations. However, when the precipitation rate is greater than 10 mm day^{-1}, the ERA5 precipitation rate is less than that in the observations. In these two months, the total precipitation from observations is 182.52 mm, which is less than that from ERA5, at 268.68 mm. In addition, the hourly averaged precipitation intensity in ERA5 reaches its maximum at 2100 BT, which is 3 h ahead of that in the observations. The ERA5 precipitation is larger than that in the observations, which is consistent with previous research (Su et al., 2013).

Figure 3 shows the diurnal variation of the equivalent reflectivity factor from the Ka-band millimeter-wave cloud radar at Yushu station on precipitation days and non-precipitation days during the observation period. During the nighttime on precipitation days, the height of the equivalent reflectivity factor exceeds 14 km AGL, with a maximum value from 2100 to 2300 BT (Fig. 3a). However, the height of the equivalent reflectivity factor is lower than 12 km during the nighttime on non-precipitation days. During the daytime on non-precipitation days, the maximum equivalent reflectivity factor is about 10 dBZ at the height of 1 km AGL (Fig. 3b). There are few clouds during most of the daytime, meaning that there is little blocking of solar radiation. On precipitation and non-precipitation days, the height of the equivalent reflectivity factor at nighttime is higher than that in the daytime.

The CBH from the cloud radar in the daytime is larger than that at nighttime (Fig. 4a). The CBH averaged on non-precipitation days is higher than on precipitation days, and the maximum CBH is lower than 2500 m AGL. The CBH at night on non-precipitation and precipitation days is similar. On precipitation days, the maximum CBH is 2200 m AGL at 1600 BT, and the minimum is 1000 m AGL at 0500 BT; while on non-precipitation days, the maximum CBH is 2200 m AGL at 1600 BT, and the minimum is 1000 m AGL at 0500 BT. On all days, the maximum CBH is 2100 m AGL at 1600 BT, and the minimum is 1000 m AGL at 0500 BT.

The CTH in the daytime is lower than that at nighttime (Fig. 4b), and is higher on precipitation days than on non-precipitation days, especially from sunset to midnight. On precipitation days, the minimum CTH is 6200 m AGL at 1200 BT, while the maximum is 11,500 m AGL at 2100 BT. On non-precipitation days, the minimum CTH is 2500 m AGL at 1600 BT, and the maximum is 7200 m at 0100 BT. On all days, the minimum CTH is 5100 m AGL at 1600 BT, and the maximum is 8100 m AGL at 0100 BT. The diurnal variation of LWC is similar

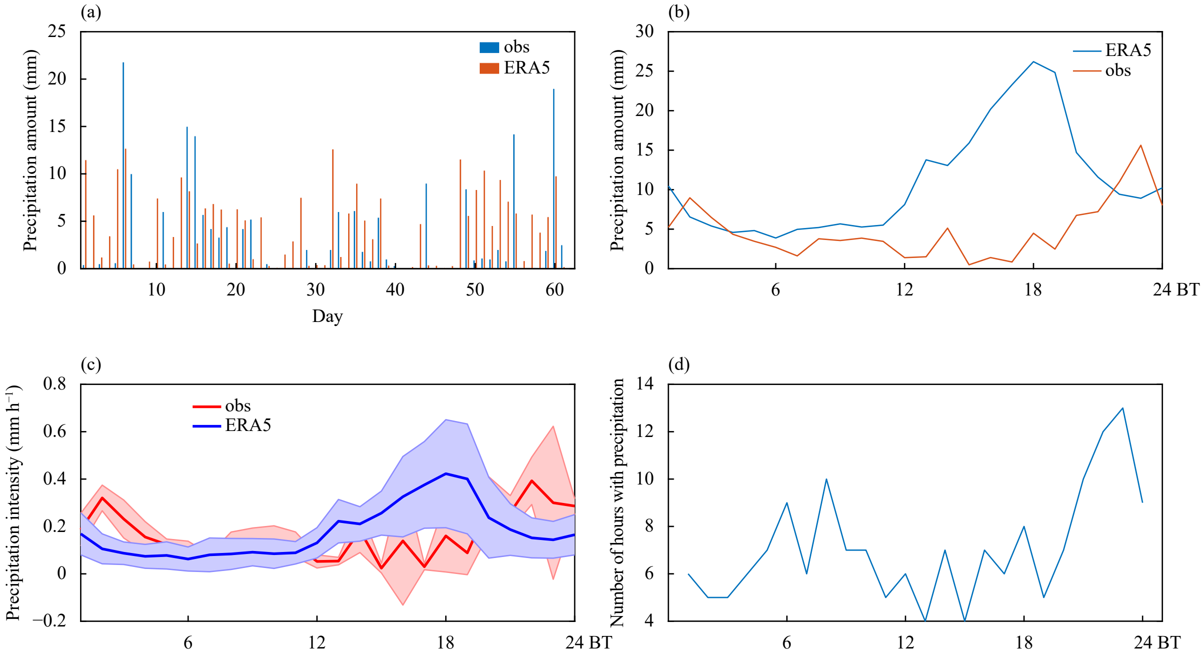

Fig. 2. (a) Time series of precipitation during the observation period from 1 July to 31 August 2019, and diurnal variations of (b) precipitation amount, (c) 1-h averaged precipitation intensity (red line for observations and blue line for ERA5 dataset) with standard deviation (red shading for observations and blue shading for ERA5 dataset), and (d) number of hours with precipitation.

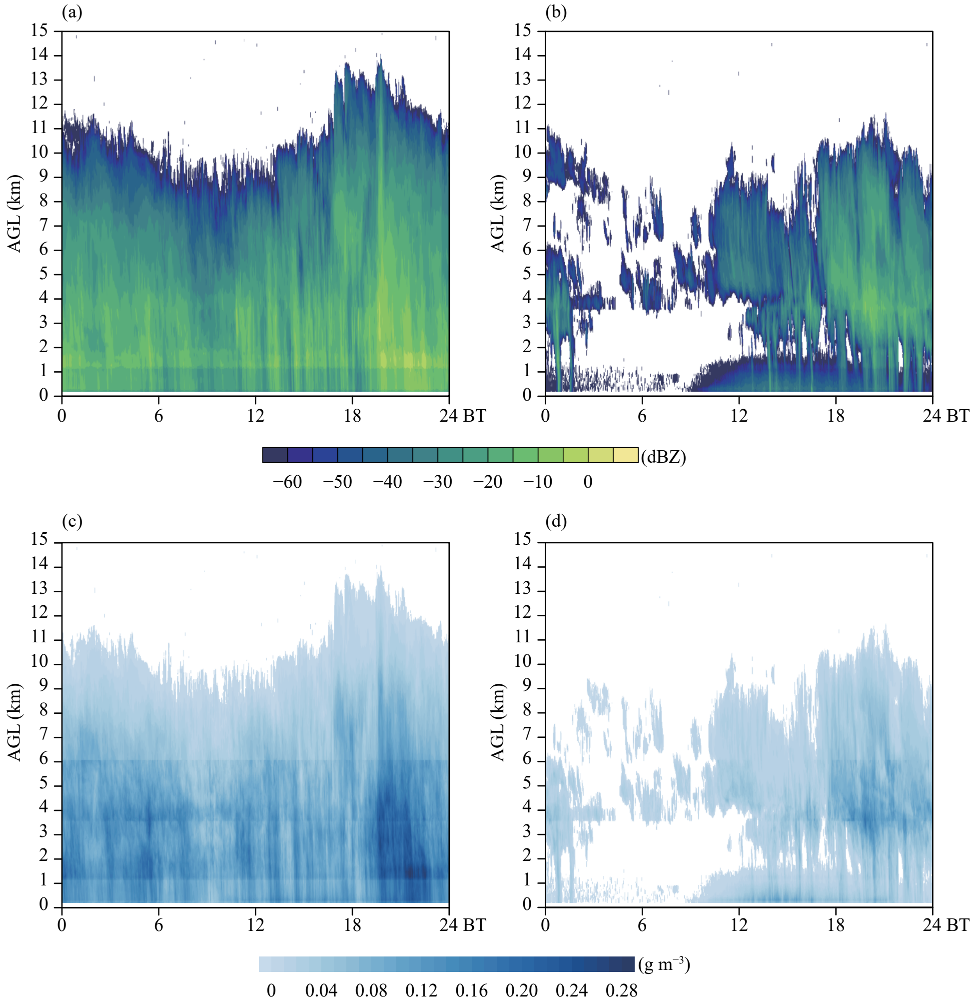

Fig. 3. Diurnal variations of (a, b) equivalent reflectivity factor along with (c, d) the liquid water content on (a, c) precipitation days and (b, d) non-precipitation days.

to that of equivalent reflectivity factor (Fig. 4c). On precipitation days, the LWC reaches a maximum, with a value of 0.28 g cm^{-3}, during 1900–2300 BT, and is mainly focused within 1–5 km AGL, which is consistent with the maximum precipitation.

On both precipitation and non-precipitation days, the dewpoint spread remains stable during 0000–0600 BT, with a value of 2°C. It then increases from 0600 BT to a maximum at 1800 BT, with a value of 3°C, which lags behind the CBH by 3–4 h, and then decreases (Fig. 5a). The dewpoint spread on non-precipitation days is larger than that on precipitation days from late afternoon to

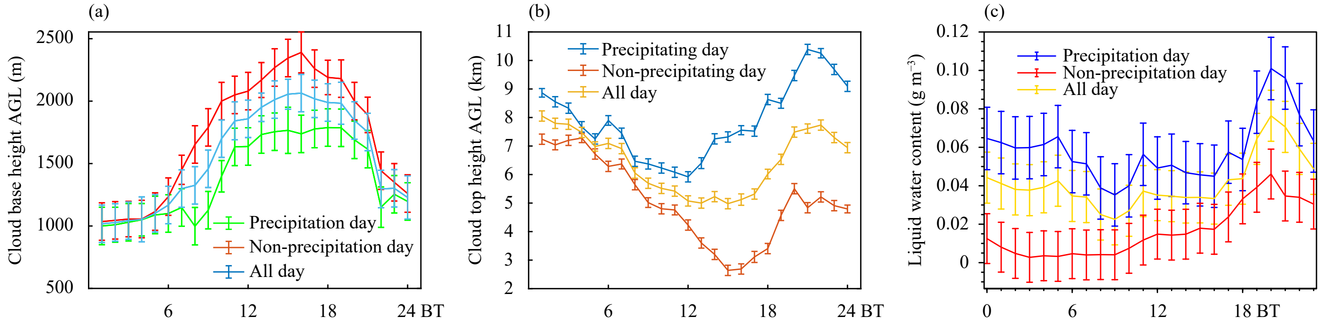

Fig. 4. Diurnal variations of (a) cloud base height, (b) cloud top height, and (c) liquid water content AGL with standard deviation (error bars) averaged on all days, non-precipitation days, and precipitation days during observation period.

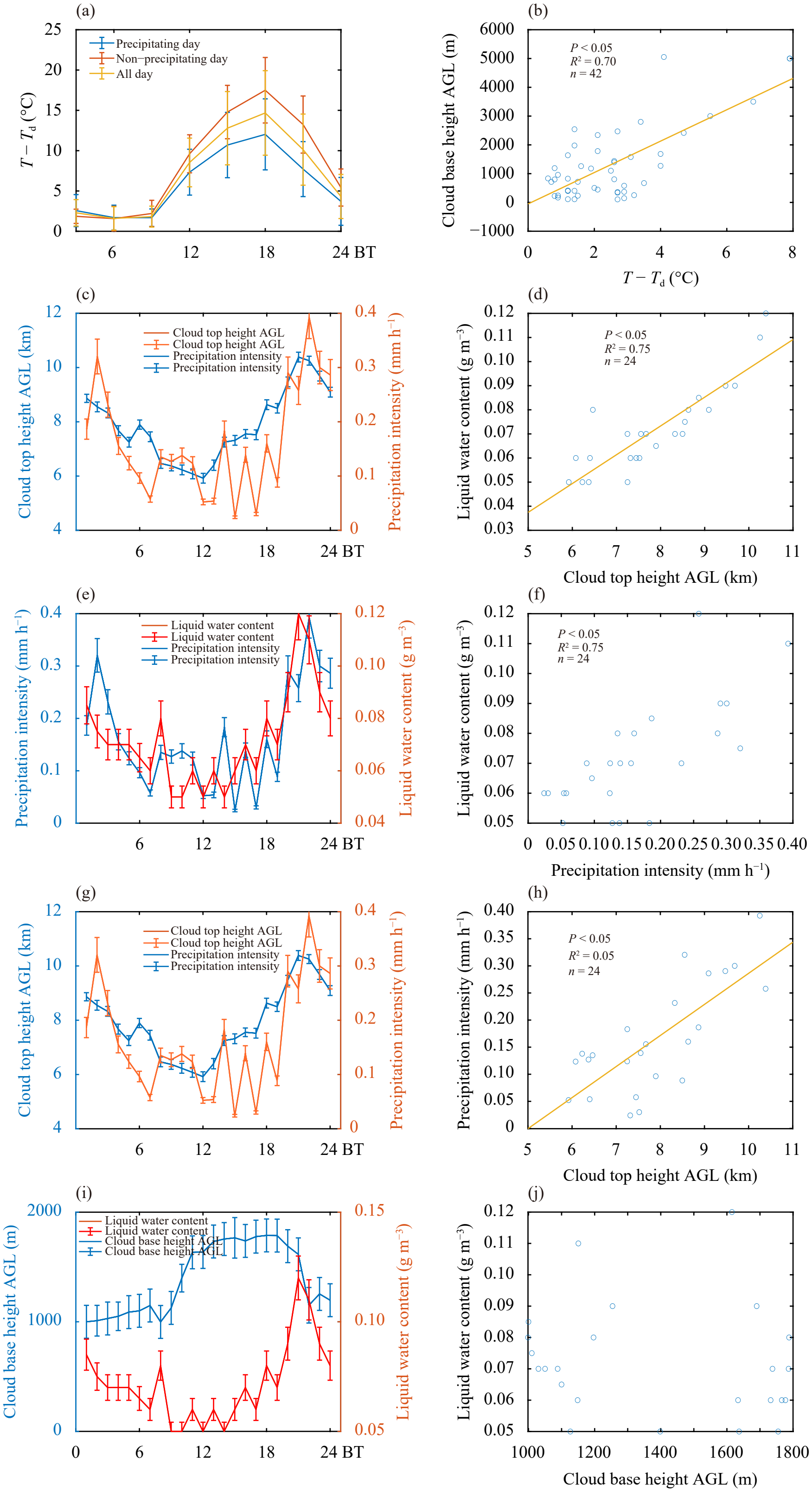

Fig. 5. Diurnal variations of (a) dewpoint spread averaged on precipitation, non-precipitation, and all days; diurnal variations of (c) CTH AGL, (e) LWC, (g) precipitation intensity, and (i) CBH AGL averaged on precipitation days. Correlations between (b) dewpoint spread and CBH ASL, (d) CTH AGL and LWC, (f) precipitation intensity and LWC, (h) CTH AGL and precipitation intensity, and (j) CBH AGL and LWC averaged on precipitation days. The error bars are the standard deviation.

early nighttime. The average dewpoint spread on precipitation days is correlated with the CBH, and the correlation coefficient reaches 0.7 with a 5% significance level (Fig. 5b). Theoretically, the height of the LCL can be calculated as $z_{\mathrm{LCL}} = 123(T - T_{\mathrm{d}})$, where the LCL is determined by the dewpoint spread. Some studies have shown that the CBH is close to the LCL (e.g., Craven et al., 2002). Therefore, the dewpoint spread makes a profound contribution to the CBH. The correlation between the LWC and CTH and precipitation intensity is at the 5% significance level, and the correlation coefficients reach 0.75 (Fig. 5d) and 0.52 (Fig. 5f), respectively. However, the correlation between the LWC and CBH is not at the 5% significance level (Fig. 5j). Therefore, the LWC is a key factor affecting the CTH and precipitation intensity.

4.2 *Thermal effects on precipitation at Yushu*

On precipitation days, the BLH increases from 0800 to 1500 BT, reaching a maximum of 1600 m AGL, and then decreases from 1500 to 2100 BT (Fig. 6a). On non-precipitation days, the BLH increases from 0800 to 1600 BT, reaching a maximum of 1900 m AGL, and then decreases from 1500 to 2100 BT (Fig. 6b). Figures 6c and 6d show the diurnal variation of the vertical profile of near-surface air temperature, revealing that the air temperature at night is lower than during the day, and that the temperature on precipitation days is less than that on non-precipitation days. On precipitation days, the decreasing rate of temperature with height is 6.5°C km^{-1} (Fig. 6c), which is due to less cloud cover in the daytime on non-precipitation days. The downward solar radiation on precipitation days is smaller than on non-precipitation days. The air temperature on non-precipitation days reaches a maximum of 15°C at 1500–2000 BT below 600 hPa (Fig. 6d), which is 3–4 h ahead of the maximum precipitation intensity. On non-precipitation days, the decreasing rate of temperature with height is 11.5°C km^{-1}, indicating super adiabatic heating to the atmosphere leading to an updraft in the boundary layer (Fig. 6d).

Figure 7 shows a combination of the temperature and vertical velocity field, averaged along a cross-section during the observation period at different moments. It is created from points E to F in the northwest–southeast direction. As can be seen in Fig. 1b, the Yushu observation site is in a basin. On precipitation days, upward motion occurs over the basin at 0000 BT (Fig. 7a), and the upward velocity at 0000 BT is larger than that at 1200 BT (Figs. 7a, b), which corresponds to the high precipitation intensity (Fig. 2c). The upward motion at night on non-precipitation days is weaker than that on precipitation days (Figs. 7a, c). At 1200 BT, there is stronger downward motion on non-precipitation days than on precipita-

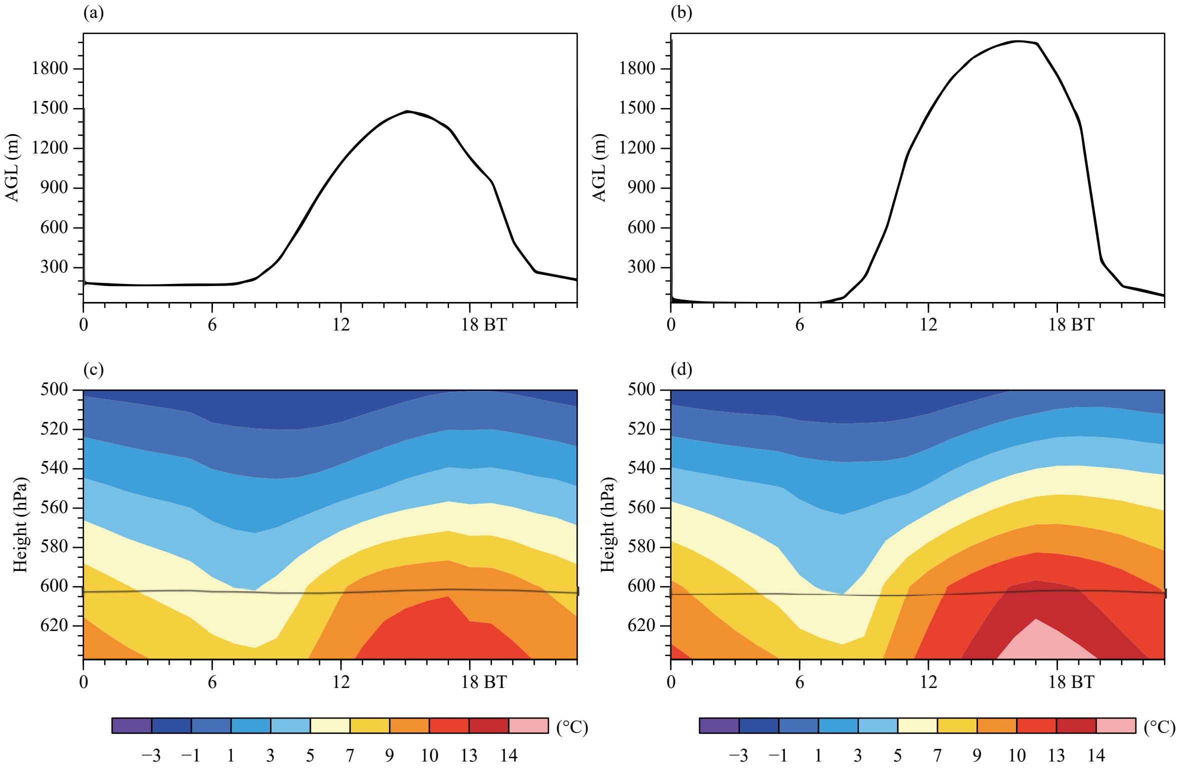

Fig. 6. Diurnal variations of (a, b) boundary layer height and (c, d) time–height contoured temperature by altitude diagrams on (a, c) precipitation and (b, d) non-precipitation days from ERA5 data.

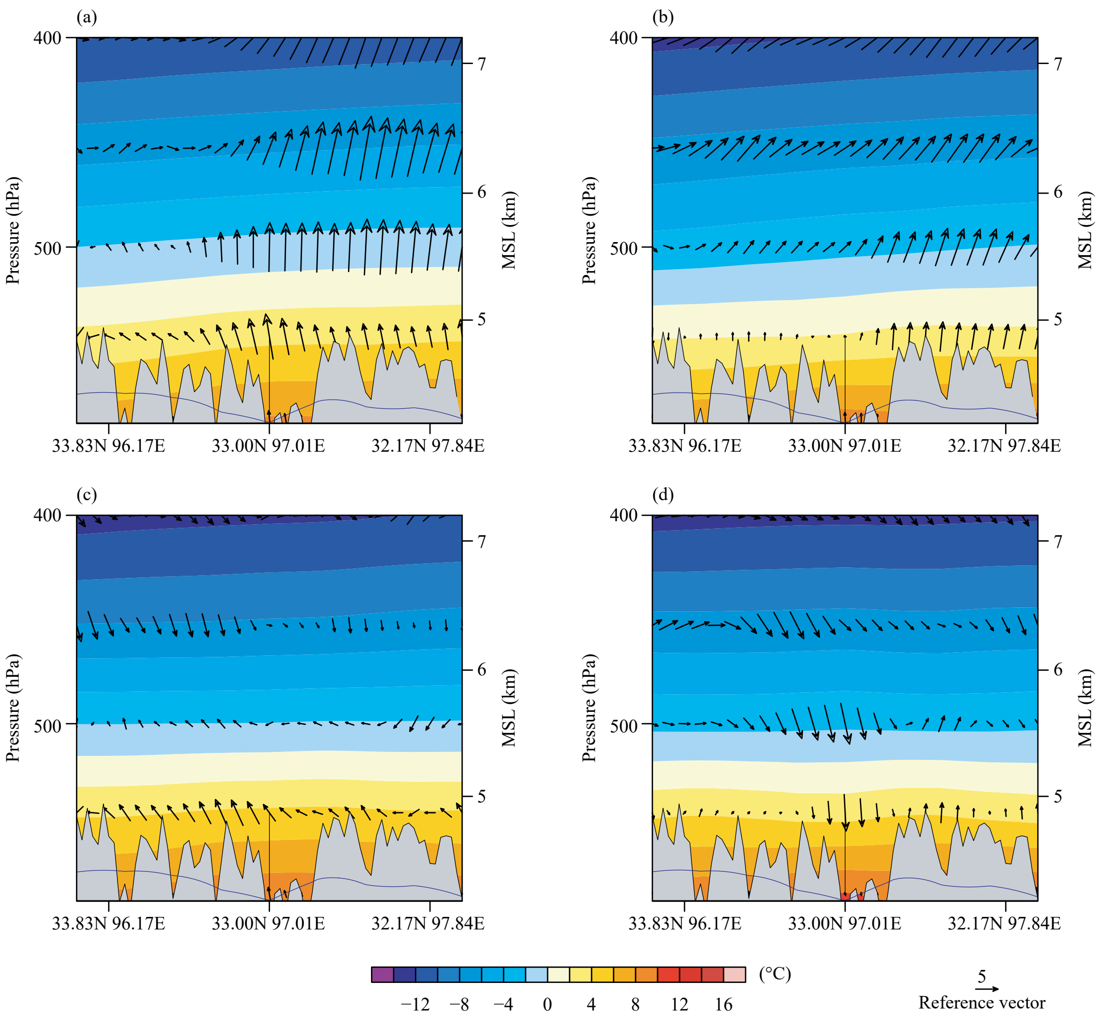

Fig. 7. Cross-sections of temperature (color-shaded) and vertical velocity (arrows) at (a, c) 0000 and (b, d) 1200 BT on (a, b) precipitation and (c, d) non-precipitation days from ERA5 data.

tion days between 500 and 400 hPa (Figs. 7b, d). The downward motion is controlled by anticyclonic circulation over the TP on non-precipitation days without other weather systems such as mesoscale TP vortices, which is consistent with the results of Wu et al. (2015). In addition, the layer between 500 and 400 hPa is above BLH, which is not controlled by the surface heating.

4.3 *Westerly jet in the upper level and oscillation of the wind direction in the lower level*

To investigate other key factors involved in forming the high cloud, the diurnal variations of the profile of u and v at 0200, 0800, 1400, and 2000 BT on precipitation and non-precipitation days are shown in Fig. 8. On both precipitation and non-precipitation days, there is a westerly jet near 200 hPa (Figs. 8a–c). The v-wind is mainly from the north in the upper level, but from the south in the lower level on precipitation days (Fig. 8b), while there is northerly wind on non-precipitation days (Fig. 8d). The average height of 200 hPa is approximately 9000 m AGL at this location. From 0800 to 0200 BT, i.e., from morning to night, the wind direction at 200 hPa remains westerly (Fig. 9). Yushu area is usually located in the south of the subtropical westerly jet (Curio et al., 2019). On precipitation days, it increases from 0700 to 1800 BT, reaching a maximum of 26 m s^{-1} (Fig. 10a). Note that 1800 BT is also the time of maximum precipitation intensity in ERA5. On non-precipitation days, the maximum wind speed is 19 m s^{-1}. The wind speed on precipitation days is larger than that on non-precipitation days. In the upper layer, the Coriolis and pressure gradient forces are balanced, which is geostrophic wind. In terms of the v-wind, there is northerly wind on non-precipitation days (Fig. 10b), while on precipitation days, there is southerly wind that reached a maximum at 1900 BT. The absolute u value is larger than v.

The average horizontal wind at 500 hPa is shown in

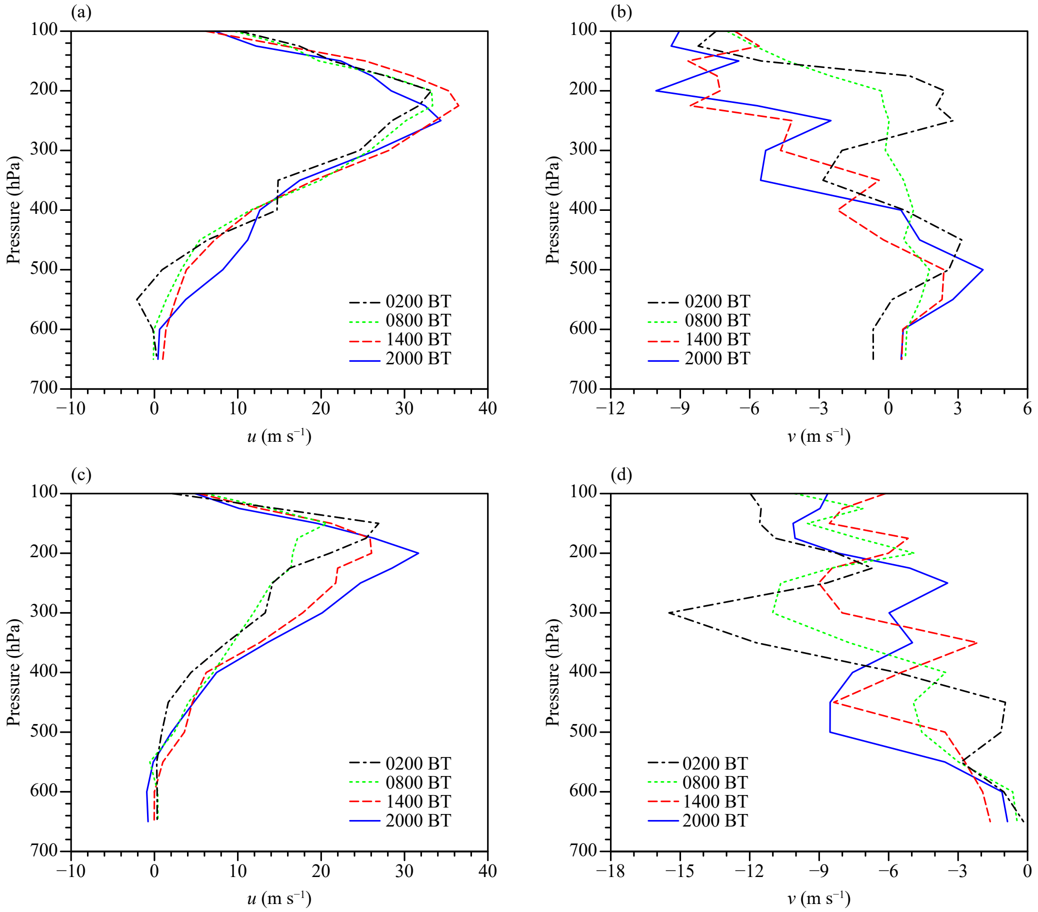

Fig. 8. Diurnal variations of (a, c) *u* and (b, d) *v* at 0200, 0800, 1400, and 2000 BT on (a, b) precipitation and (c, d) non-precipitation days from ERA5 data.

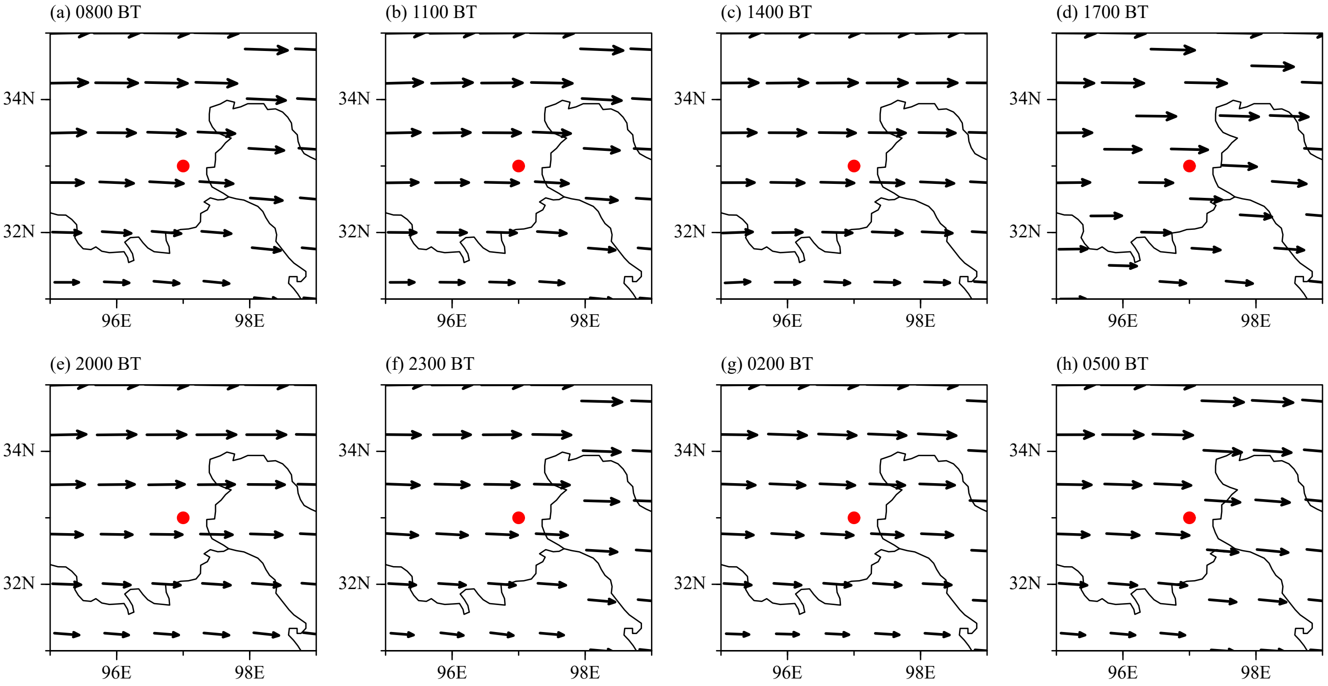

Fig. 9. Horizontal wind fields at 200 hPa at (a) 0800, (b) 1100, (c) 1400, (d) 1700, (e) 2000, (f) 2300, (g) 0200, and (h) 0500 BT from ERA5 data. The red dot represents the location of Yushu.

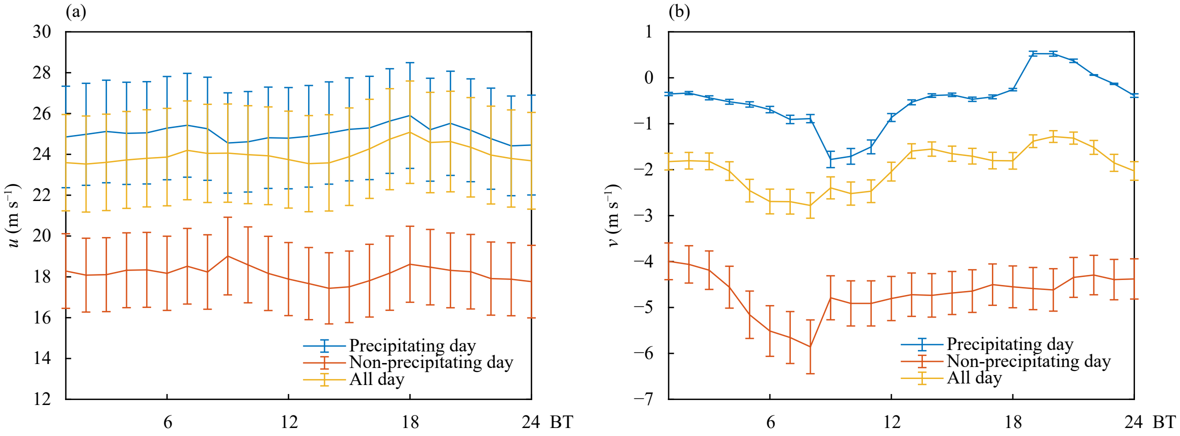

Fig. 10. Diurnal variations of (a) *u* and (b) *v* at 200 hPa from ERA5 data. The error bars are the standard deviation.

Fig. 11. The wind direction changes from westerly and eventually back to northerly from early morning to noon and into the night and the following morning. Based on radiosonde data at Yushu, the average 500-hPa height is about 2000 m AGL, and based on ERA5 data, the average BLH is about 2000 m (Fig. 7). Therefore, the 500-hPa height is below the BLH, where the wind is influenced by the Coriolis force, turbulent shear stress, and the pressure gradient force. The results in Fig. 12 suggest that the clockwise oscillation of the boundary layer winds may be explained by the response of the atmosphere to a diurnally heated surface (Holton, 1967). In previous studies (e.g., Holton, 1967), the cycle of oscillation is 17–24 h, which is related to the Coriolis coefficient. In this study, there is clearly a clockwise oscillation of horizontal wind with a cycle of approximately 1 day at 500 hPa on precipitation days, non-precipitation days, and all days (Fig. 12). However, there are differences under different weather conditions. On precipitation days, there is northeasterly wind, while it is mainly southwesterly wind on non-precipitation days (Fig. 12a). The *u*- and *v*-wind are different at different times. The *u*-wind is from the east on precipitation days, which is the largest at 0600 BT and smallest at 1500 BT. On non-precipitation days, however, *u* is the strongest from the east at 0600 BT and then changes to be strongest from the west at 1500 BT (Fig. 12b). On precipitation days, *v* is northerly throughout the day. It decreases from 0600 BT,

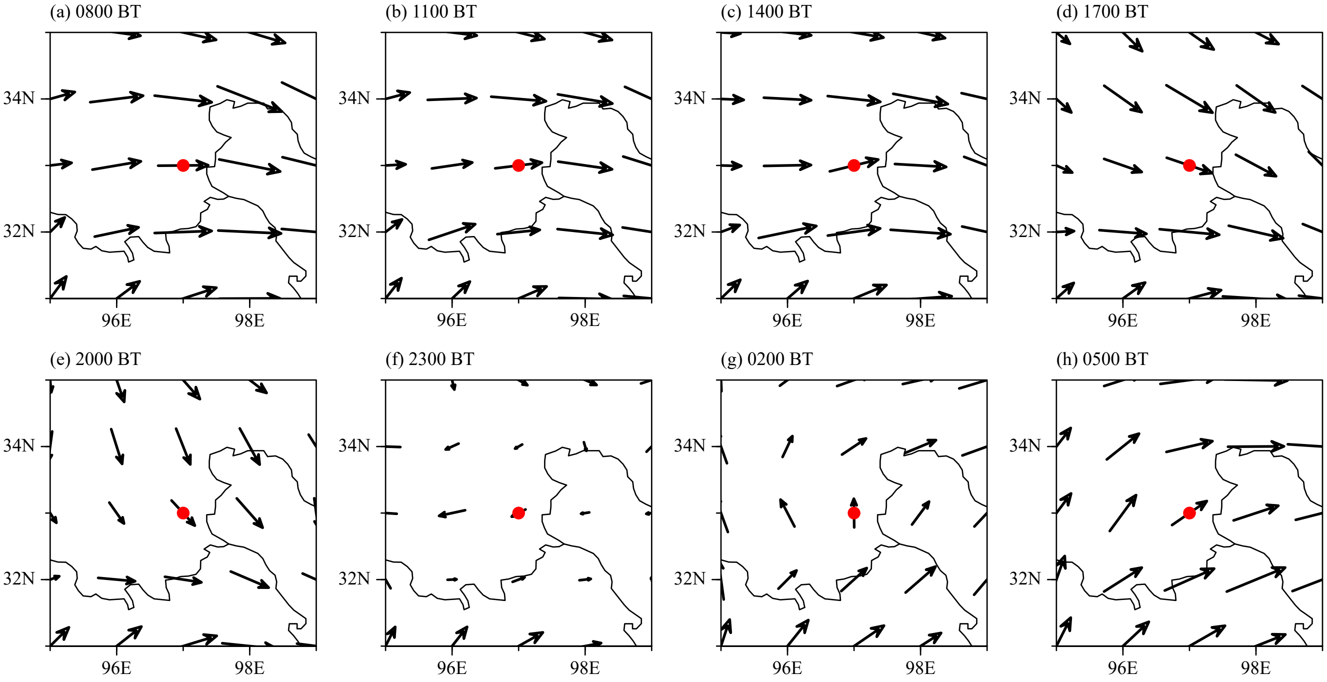

Fig. 11. As in Fig. 9, but for 500 hPa.

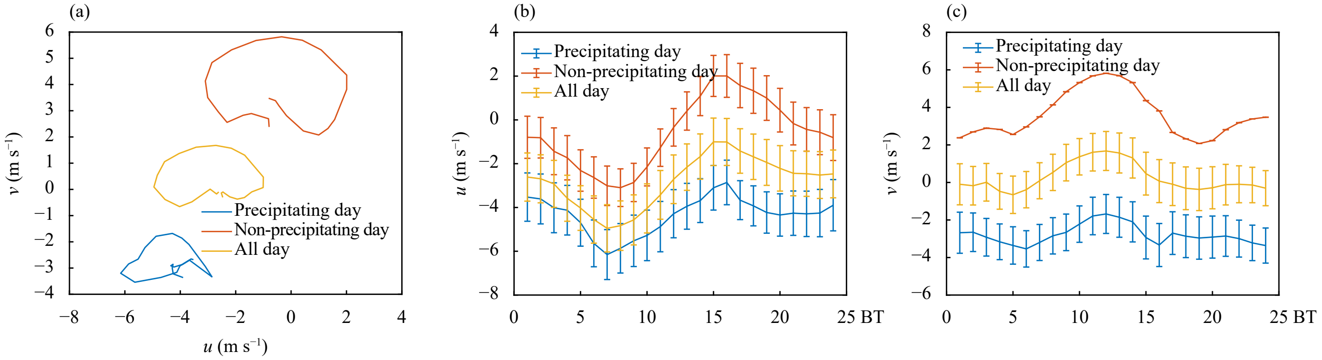

Fig. 12. Diurnal circles of (a) the horizontal wind speed at 500 hPa, (b) u, and (c) v averaged on precipitation days, non-precipitation days, and all days from ERA5 data.

reaches a minimum at 1200 BT, and then increases to a maximum at 2000 BT. On non-precipitation days, it is a southerly wind throughout the day. It reaches a minimum at 0600 BT, then increases to a maximum at 1200 BT, and finally decreases to a minimum at 1900 BT (Fig. 12c).

On precipitation days, the integral of water vapor flux from plane A is negative, while from planes B, C, and D, it is positive, suggesting that the water vapor enters Yushu area from planes A, C, and D, but exits via plane B (Fig. 13). From the spatial distribution of water vapor flux, the water vapor transport is mainly from the west, reaching a maximum value between 2100 and 2300 BT (Figs. 13, 14), which occurs at the same time as the LWC from the cloud radar observations. To investigate the relationship between the water vapor transport and westerly wind, the difference (ΔV) in horizontal wind speed between 200 and 500 hPa is calculated (Fig. 15a): $\Delta V = (u_{200} - u_{500})^2 + (v_{200} - v_{500})^2$, where u_{200} and v_{200} are u and v at 200 hPa, and u_{500} and v_{500} are u and v at 500 hPa. The results show that the diurnal variation of ΔV is consistent with the precipitation intensity. At 2100 BT, the westerly jet at 200 hPa becomes strengthened, and the easterly wind becomes largest at 500 hPa. The largest ΔV results in the unstable condition. The variable ΔV correlates positively with water vapor transport at the 5% significance level, and has a profound impact on the water vapor transport.

The diurnal variation of vertical velocity on precipitation days increases from morning to the afternoon, reaching a maximum at 1100 BT. The maximum vertical velocity is 3–4 h ahead of the precipitation intensity. The correlation coefficient reaches 0.9 at the 5% significance level. CAPE increases from morning to afternoon, reaching a maximum at 1900 BT with a value of 450 J kg^{-1}, and then decreases to less than 100 J kg^{-1} (Fig. 15c). According to the analysis of the lead–lag relationship, the maximum CAPE is 3–4 h ahead of the precipitation intensity. The correlation coefficient reaches 0.8 at the 5% significance level (Fig. 15b).

5. Summary

The cloud precipitation process over the TP has attracted much attention. However, there is a knowledge gap in understanding the characteristics of cloud precipitation in the northeastern TP, due to the scarcity of observation data. Using data from cloud radar, ground observations, and ERA5 reanalysis data, the factors influencing nighttime precipitation during summer in the Yushu area of

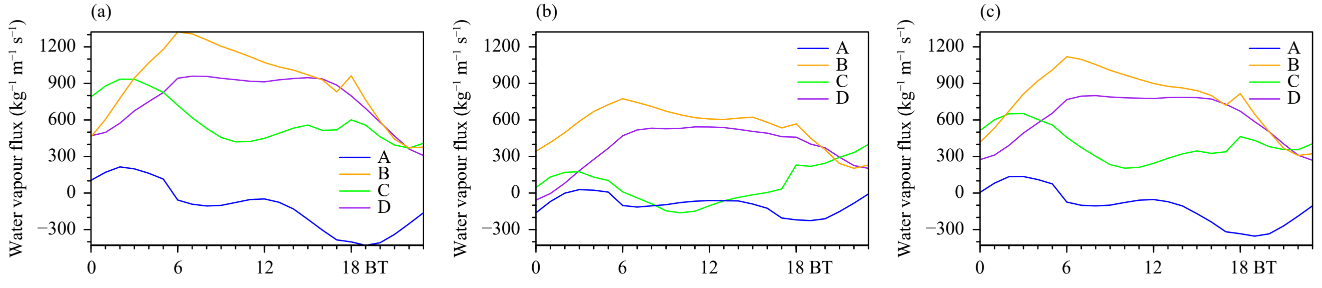

Fig. 13. Diurnal variations of the integral of water vapor flux on (a) precipitation days, (b) non-precipitation days, and (c) all days from ERA5 data. Letters A, B, C, and D refer to as the planes in Fig. 1b. A positive value represents water vapor transport from west to east or from south to north. A negative value represents water vapor transport from east to west or from north to south.

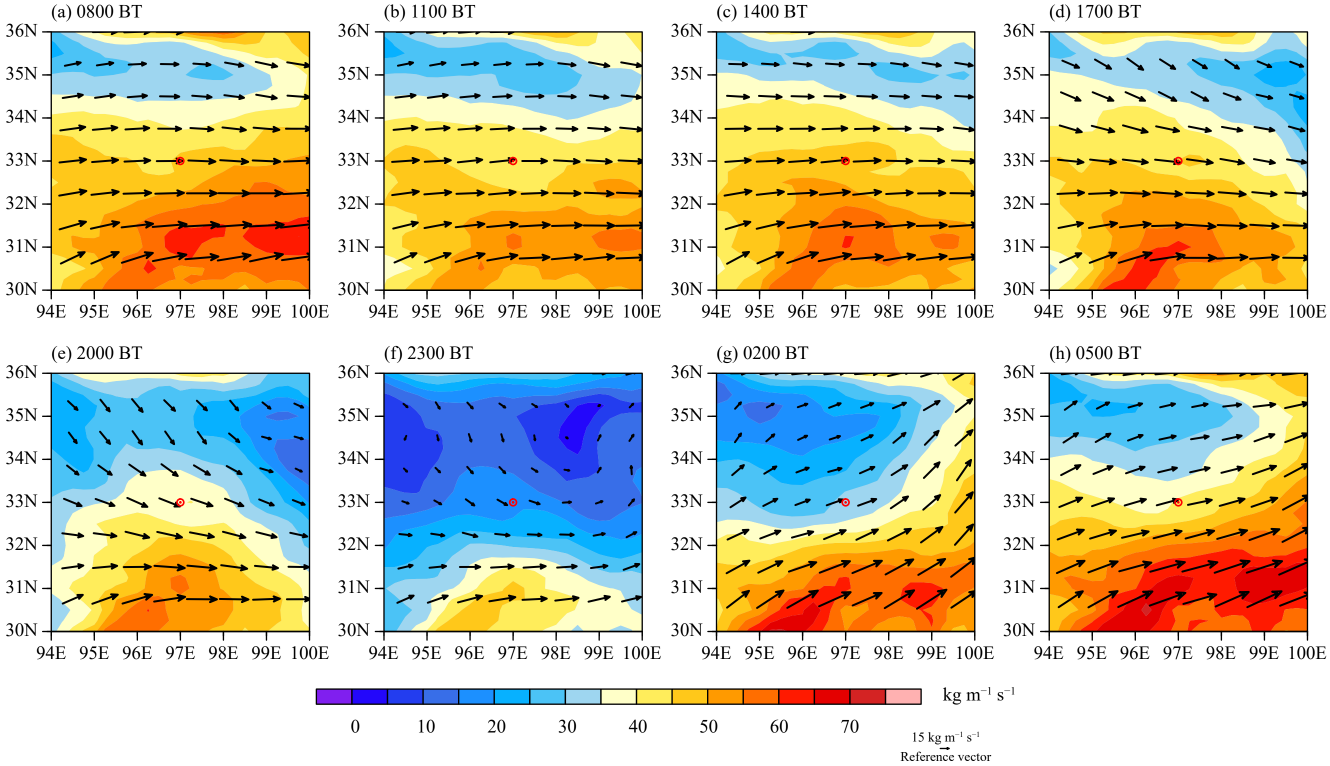

Fig. 14. Diurnal variations of the integral of water vapor flux at (a) 0800, (b) 1100, (c) 1400, (d) 1700, (e) 2000, (f) 2300, (g) 0200, and (h) 0500 BT from ERA5 data.

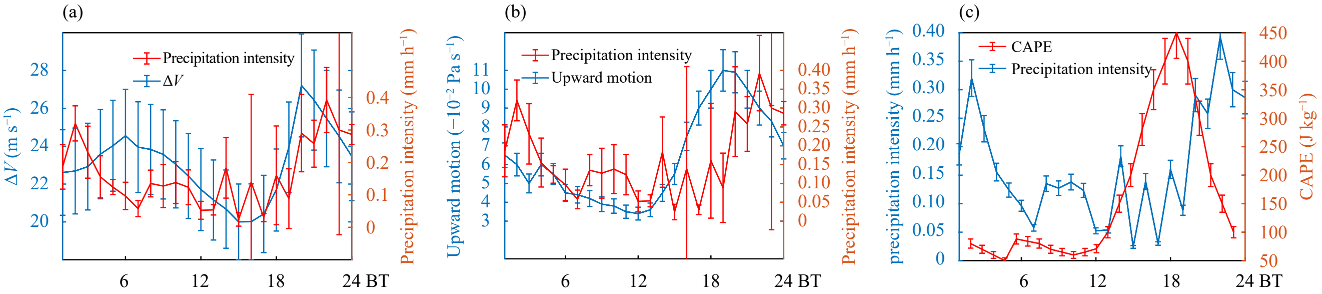

Fig. 15. Diurnal variations of (a) Δ*V*, (b) vertical velocity, and (c) CAPE from ERA5 data versus the precipitation intensity from observation.

the TP are investigated. Non-precipitation and precipitation days are compared. The results show that the average CTH over Yushu is below 10 km in the daytime on precipitation days, whereas it is more than 10 km at night, and is at its highest at 2300 BT. The average dewpoint spread on precipitation days is correlated with the CBH, with the correlation coefficient reaching 0.7 at the 5% significance level and demonstrating that the dewpoint spread has a profound impact on the CBH. The correlation between the LWC and CTH and precipitation is at the 5% significance level, with the correlation coefficients reaching 0.75 and 0.52, respectively, highlighting that the LWC makes a large contribution to the precipitation and CTH.

Diurnally, the maximum precipitation intensity is at 2300 BT, which lags behind the CAPE in ERA5 by 3 h. There is downward motion in the mid day on non-precipitation days, while there is upward motion at night on precipitation days. In addition, the horizontal wind direction in the lower level (below 5000 m) rotates clockwise from morning to night. Wind shear occurs in the mid atmosphere, accompanied by a subtropical westerly jet in the upper level. The difference in horizontal wind speed between 200 and 500 hPa is positively related to the water vapor transport, thereby contributing to the formation of upper-level clouds.

It is important to acknowledge that the spatial resolution of the ERA5 data (31 km) is a major issue, as it is too coarse to take into account the topographical features of the region. Therefore, the details of local circulation systems most likely will not be represented. Data with a finer spatial resolution are required to investigate the diurnal cycle in future research. In addition, numerical simulations are also needed to investigate the precipitation patterns caused by localized thermal convection or by the propagation of mesoscale TP vortices.

Acknowledgments. The ERA5 data employed in this study are available from https://www.ecmwf.int/en/forecasts/datasets/reanalysis-datasets/era5.

REFERENCES

Bai, A.-J., C.-H. Liu, and X.-D. Liu, 2008: Diurnal variation of summer rainfall over the Tibetan Plateau and its neighboring regions revealed by TRMM multi-satellite precipitation analysis. *Chinese J. Geophys.*, **51**, 518–529, doi: 10.1002/cjg2.1242.

Beljaars, A. C. M., A. R. Brown, and N. Wood, 2004: A new parametrization of turbulent orographic form drag. *Quart. J. Roy. Meteor. Soc.*, **130**, 1327–1347, doi: 10.1256/qj.03.73.

Cadeddu, M. P., J. C. Liljegren, and D. D. Turner, 2013: The atmospheric radiation measurement (ARM) program network of microwave radiometers: Instrumentation, data, and retrievals. *Atmos. Meas. Tech.*, **6**, 2359–2372, doi: 10.5194/amt-6-2359-2013.

Chang, Y., and X. L. Guo, 2016: Characteristics of convective cloud and precipitation during summer time at Naqu over Tibetan Plateau. *Chinese Sci. Bull.*, **61**, 1706–1720, doi: 10.1360/N972015-01292. (in Chinese)

Chen, G. X., W. M. Sha, and T. Iwasaki, 2009: Diurnal variation of precipitation over southeastern China: 2. Impact of the diurnal monsoon variability. *J. Geophys. Res. Atmos.*, **114**, D21105, doi: 10.1029/2009JD012181.

Chen, H. P., J. Q. Sun, and K. Fan, 2012: Decadal features of heavy rainfall events in eastern China. *Acta Meteor. Sinica*, **26**, 289–303, doi: 10.1007/s13351-012-0303-0.

Chen, M., M. X. Chen, and S. Y. Fan, 2014: The real-time radar radial velocity 3DVar assimilation experiments for application to an operational forecast model in North China. *Acta Meteor. Sinica*, **72**, 658–677, doi: 10.11676/qxxb2014.070. (in Chinese)

Craven, J. P., R. E. Jewell, and H. E. Brooks, 2002: Comparison between observed convective cloud-base heights and lifting condensation level for two different lifted parcels. *Wea. Forecasting*, **17**, 885–890, doi: 10.1175/1520-0434(2002)017<0885:CBOCCB>2.0.CO;2.

Curio, J., R. Schiemann, K. I. Hodges, et al., 2019: Climatology of Tibetan Plateau vortices in reanalysis data and a high-resolution global climate model. *J. Climate*, **32**, 1933–1950.

Feng, J. M., L. P. Liu, Z. J. Wang, et al., 2002: The statistic characteristics of radar echo and precipitation and some thermodynamic variables in Qinghai–Xizang Plateau. *Plateau Meteor.*, **21**, 368–374, doi: 10.3321/j.issn:1000-0534.2002.04.005. (in Chinese)

Feng, L., and F. Y. Wei, 2008: Regional characteristics of summer precipitation on Tibetan Plateau and its water vapor feature in neighboring areas. *Plateau Meteor.*, **27**, 491–499. (in Chinese)

Fu, Y. F., G. S. Liu, G. X. Wu, et al., 2006: Tower mast of precipitation over the central Tibetan Plateau summer. *Geophys. Res. Lett.*, **33**, L05802, doi: 10.1029/2005GL024713.

Fu, Y. F., Y. M. Ma, L. Zhong, et al., 2020: Land-surface processes and summer-cloud-precipitation characteristics in the Tibetan Plateau and their effects on downstream weather: A review and perspective. *Natl. Sci. Rev.*, **7**, 500–515, doi: 10.1093/nsr/nwz226.

Fujinami, H., and T. Yasunari, 2001: The seasonal and intraseasonal variability of diurnal cloud activity over the Tibetan Plateau. *J. Meteor. Soc. Japan*, **79**, 1207–1227, doi: 10.2151/jmsj.79.1207.

Gong, Y. F., L. R. Ji, and T. Y. Duan, 2004: Precipitation character of rainy season of Qinghai–Xizang Plateau and onset over East Asian monsoon. *Plateau Meteor.*, **23**, 313–322. (in Chinese)

Guo, J. P., J. Zhang, K. Yang, et al., 2021: Investigation of near-global daytime boundary layer height using high-resolution radiosondes: First results and comparison with ERA5, MERRA-2, JRA-55, and NCEP-2 reanalyses. *Atmos. Chem. Phys.*, **21**, 17,079–17,097, doi: 10.5194/acp-21-17079-2021.

Holton, J. R., 1967: The diurnal boundary layer wind oscillation above sloping terrain. *Tellus*, **19**, 200–205, doi: 10.3402/tellusa.v19i2.9766.

Ji, X. L., H. M. Wu, A. N. Huang, et al., 2017: Characteristics of the precipitation diurnal variation over Qinghai–Tibetan Plateau in summer. *Plateau Meteor.*, **36**, 1188–1200, doi: 10.7522/j.issn.1000-0534.2016.00119. (in Chinese)

Li, P. X., K. Furtado, T. J. Zhou, et al., 2021: Convection-permitting modelling improves simulated precipitation over the central and eastern Tibetan Plateau. *Quart. J. Roy. Meteor. Soc.*, **147**, 341–362, doi: 10.1002/qj.3921.

Liu, L. P., J. M. Feng, R. Z. Chu, et al., 2002: The diurnal variation of precipitation in monsoon season in the Tibetan Plateau. *Adv. Atmos. Sci.*, **19**, 365–378, doi: 10.1007/s00376-002-0028-6.

Romps, D. M., 2017: Exact expression for the lifting condensation level. *J. Atmos. Sci.*, **74**, 3891–3900, doi: 10.1175/JAS-D-17-0102.1.

Su, F. G., X. L. Duan, D. L. Chen, et al., 2013: Evaluation of the global climate models in the CMIP5 over the Tibetan Plateau. *J. Climate*, **26**, 3187–3208, doi: 10.1175/JCLI-D-12-00321.1.

Sun, Y., and C. F. Zhao, 2020: Influence of Saharan dust on the large-scale meteorological environment for development of tropical cyclone over North Atlantic Ocean Basin. *J. Geophys. Res. Atmos.*, **125**, e2020JD033454, doi: 10.1029/2020JD033454.

Tao, S.-Y., and Y.-H. Ding, 1981: Observational evidence of the influence of the Qinghai–Xizang (Tibet) Plateau on the occurrence of heavy rain and severe convective storms in China. *Bull. Amer. Meteor. Soc.*, **62**, 23–30, doi: 10.1175/1520-0477(1981)062<0023:OEOTIO>2.0.CO;2.

Troen, I. B., and L. Mahrt, 1986: A simple model of the atmospheric boundary layer; sensitivity to surface evaporation. *Boundary-Layer Meteorol.*, **37**, 129–148, doi: 10.1007/BF00122760.

Uyeda, H., H. Yamada, J. Horikomi, et al., 2001: Characteristics of convective clouds observed by a Doppler radar at Naqu on Tibetan Plateau during the GAME-Tibet IOP. *J. Meteor. Soc. Japan*, **79**, 463–474, doi: 10.2151/jmsj.79.463.

Wang, C. J., W. J. Dong, and Z. G. Wei, 2003: A study on relationship between freezing-thawing processes of the Qinghai-Xizang Plateau and the atmospheric circulation over East

Asia. *Chinese J. Geophys.*, **46**, 438–448, doi: 10.1002/cjg2.3361.

Wang, X. J., G. J. Pang, and M. X. Yang, 2018: Precipitation over the Tibetan Plateau during recent decades: A review based on observations and simulations. *Int. J. Climatol.*, **38**, 1116–1131, doi: 10.1002/joc.5246.

Wang, Y., Y. Yang, and C. H. Wang, 2014: Improving forecasting of strong convection by assimilating cloud-to-ground lightning data using the physical initialization method. *Atmos. Res.*, **150**, 31–41, doi: 10.1016/j.atmosres.2014.06.017.

Wang, Y., C. F. Zhao, Z. P. Dong, et al., 2018: Improved retrieval of cloud base heights from ceilometer using a non-standard instrument method. *Atmos. Res.*, **202**, 148–155, doi: 10.1016/j.atmosres.2017.11.021.

Wu, G. X., A. M. Duan, Y. M. Liu, et al., 2015: Tibetan Plateau climate dynamics: Recent research progress and outlook. *Natl. Sci. Rev.*, **2**, 100–116, doi: 10.1093/nsr/nwu045.

Xia, Y., Y. W. Wang, Y. Huang, et al., 2021: Significant contribution of stratospheric water vapor to the poleward expansion of the Hadley circulation in autumn under greenhouse warming. *Geophys. Res. Lett.*, **48**, e2021GL094008, doi: 10.1029/2021GL094008.

Xu, W. X., and E. J. Zipser, 2011: Diurnal variations of precipitation, deep convection, and lightning over and east of the eastern Tibetan Plateau. *J. Climate*, **24**, 448–465, doi: 10.1175/2010JCLI3719.1.

Xu, X. D., C. G. Lu, X. H. Shi, et al., 2008: World water tower: An atmospheric perspective. *Geophys. Res. Lett.*, **35**, L20815, doi: 10.1029/2008GL035867.

Yang, K., and C. H. Wang, 2019: Water storage effect of soil freeze-thaw process and its impacts on soil hydro-thermal regime variations. *Agric. For. Meteorol.*, **265**, 280–294, doi: 10.1016/j.agrformet.2018.11.011.

Yang, Y. K., C. F. Zhao, and H. Fan, 2020: Spatiotemporal distributions of cloud properties over China based on Himawari-8 advanced Himawari imager data. *Atmos. Res.*, **240**, 104927, doi: 10.1016/j.atmosres.2020.104927.

You, Q. L., J. Z. Min, W. Zhang, et al., 2015: Comparison of multiple datasets with gridded precipitation observations over the Tibetan Plateau. *Climate Dyn.*, **45**, 791–806, doi: 10.1007/s00382-014-2310-6.

Yu, R. C., J. Li, H. M. Chen, et al., 2014: Progress in studies of the precipitation diurnal variation over contiguous China. *Acta Meteor. Sinica*, **72**, 948–968, doi: 10.11676/qxxb2014.047. (in Chinese)

Zhang, Y. H., M. Xue, K. F. Zhu, et al., 2019: What is the main cause of diurnal variation and nocturnal peak of summer precipitation in Sichuan Basin, China? The key role of boundary layer low-level jet inertial oscillations. *J. Geophys. Res. Atmos.*, **124**, 2643–2664, doi: 10.1029/2018JD029834.

Zhang, Y. Y., and S. A. Klein, 2013: Factors controlling the vertical extent of fair-weather shallow cumulus clouds over land: Investigation of diurnal-cycle observations collected at the ARM Southern Great Plains site. *J. Atmos. Sci.*, **70**, 1297–1315, doi: 10.1175/JAS-D-12-0131.1.

Zhao, C. F., S. C. Xie, S. A. Klein, et al., 2012: Toward understanding of differences in current cloud retrievals of ARM ground-based measurements. *J. Geophys. Res. Atmos.*, **117**, D10206, doi: 10.1029/2011JD016792.

Zhao, C. F., L. P. Liu, Q. Q. Wang, et al., 2017: MMCR-based characteristic properties of non-precipitating cloud liquid droplets at Naqu site over Tibetan Plateau in July 2014. *Atmos. Res.*, **190**, 68–76, doi: 10.1016/j.atmosres.2017.02.002.

Zhao, C. F., Y. Y. Chen, J. M. Li, et al., 2019: Fifteen-year statistical analysis of cloud characteristics over China using Terra and Aqua Moderate Resolution Imaging Spectroradiometer observations. *Int. J. Climatol.*, **39**, 2612–2629, doi: 10.1002/joc.5975.

Zhao, C. F., Y. K. Yang, H. Fan, et al., 2020: Aerosol characteristics and impacts on weather and climate over the Tibetan Plateau. *Natl. Sci. Rev.*, **7**, 492–495, doi: 10.1093/nsr/nwz184.

Zhao, P., X. D. Xu, F. Chen, et al., 2017: The Third Atmospheric Scientific Experiment for understanding the earth–atmosphere coupled system over the Tibetan Plateau and its effects. *Bull. Amer. Meteor. Soc.*, **99**, 757–776, doi: 10.1175/BAMS-D-16-0050.1.

Zhou, X., K. Yang, and Y. Wang, 2018: Implementation of a turbulent orographic form drag scheme in WRF and its application to the Tibetan Plateau. *Climate Dyn.*, **50**, 2443–2455, doi: 10.1007/s00382-017-3677-y.

Tech & Copy Editor: Zhirong CHEN